On-demand nanoengineering of in-plane ferroelectric topologies

Marti Checa[1*], Bharat Pant[2], Alexander Puretzky[1], Bogdan Dryzhakov[1], Rama K. Vasudevan[1], Yongtao Liu[1], Pravin Kavle,[3,4] Arvind Dasgupta,[3,4,] Lane W. Martin[3,4,5], Ye Cao[2], Liam Collins[1], Stephen Jesse[1], Neus Domingo[1], Kyle P. Kelley[1]

[1] Center for Nanophase Materials Sciences, Oak Ridge National Laboratory, Oak Ridge, Tennessee 37831, USA.
[2] Department of Materials Science and Engineering, University of Texas at Arlington, Arlington, Texas 76019, USA.
[3] Department of Materials Science and Engineering, University of California Berkeley, Berkeley, California 94720, USA.
[4] Materials Sciences Division, Lawrence Berkeley National Laboratory, Berkeley, CA 94720, USA.
[5] Departments of Materials Science and NanoEngineering, Chemistry, and Physics and Astronomy and the Rice Advanced Materials Institute, Rice University, Houston, TX 77005, USA.

email: checam@ornl.gov

Hierarchical assemblies of ferroelectric nanodomains (or superdomains) can exhibit exotic morphologies that lead to distinct behaviors and functionalities. Controlling these superdomains reliably is critical for realizing new states with desired functional properties. Here, using a biased atomic force microscopy tip we reveal a so-called super-switching mechanism of the in-plane superdomains of a model ferroelectric $Pb_{0.6}Sr_{0.4}TiO_3$, demonstrating that the writing process is dominated by a superdomain nucleation and stabilization process. We show that the scanning-probe's trajectory enables on-demand formation of intricate center-divergent/convergent and flux-closure polar structures. Correlative piezoresponse force microscopy and optical spectroscopy confirm the topological nature and significant tunability of these emergent structures. The stability of the generated structures, validated by phase-field modeling, suggests potential for reliable multi-state nanodevice architectures, offering an alternative route for creating tunable topological structures in neuromorphic circuits, forging a new frontier in nanolithography for ferroics.

Keywords: ferroelectrics, center-divergent, flux-closure, automated SPM, topological polar structures

The drive towards miniaturization in ferroelectric materials, crucial for advancements in nanoelectronics[1,2] and neuromorphic computing[3], has led to the emergence of complex polar domain configurations[1,4-11] with new functionalities. Intricate patterns of polarization, including skyrmions[12], hopfions[7] and other topological structures, can arise naturally[13], be created by adjusting growth conditions[14-19], form through stacking of twisted freestanding layers[20], be identified in topologically confined ferroelectric domain walls[21,22], or be induced by local stimuli such as bias pulses [23], mechanical indentation[24,25], or heat-induced phase-transitions[26]. In turn, understanding and controlling ferroelectric polarization switching mechanisms at the nanoscale is essential for integrating these polar structures into next generation technologies, highlighting the intersection of fundamental science and practical applications.

For integration into electronic devices, it is crucial that these configurations are rapidly and efficiently manipulated – written, read, and erased locally and on-demand[21]. While magnetic structures[27] have been extensively studied and utilized for similar purposes[28], achieving full dynamic control over such states in ferroelectrics remains challenging[29,30]. Polar center divergent/convergent and flux-closure domains can naturally form and have been created by application of electric fields[9,23,31]. It is known that the competition between electrostatic and elastic energies is critical for the stability of the core and domain vertices, of such structures[30]. In order to facilitate the stabilization of domains at the micro- or nano-scales, a deep understanding of local-switching mechanisms and the competing energy landscapes is required.

Using thin-film epitaxy and strain engineering, it is possible to produce ferroelectric films featuring periodic nanodomains that self-assemble into larger 'superdomains' with distinct in-plane polarization[32-34], and, here, these structure serve as an ideal platform for exploring these phenomena. Prior studies have demonstrated in-plane polarization switching in such systems

through the use of an atomic force microscopy (AFM)-biased tip[32], wherein it was hypothesized that the slow-scan direction produces a "trailing" electric field responsible for driving local polarization rotation.[35] In this work, we demonstrate that the dynamics of superdomain nucleation and growth are more complex than previously reported.

Using a biased AFM tip, we performed intricate, non-standard movements along arbitrary scan paths – typically not offered by commercial scanning probe systems – to engineer user defined effective in-plane electric fields. This approach enabled the creation of unique spiral- and flower-like tip trajectories, effectively stabilizing center-divergent/convergent and flux-closure structures in strained $Pb_{0.6}Sr_{0.4}TiO_3$ (PSTO) films. This process revealed a complex in-plane superdomain-switching mechanism (here, referred to as super-switching), involving superdomain nucleation followed by stabilization of superdomain boundaries (or super-boundaries), emphasizing the critical role of the scan path's trajectory in shaping the final superdomain structure.

We have explored the complex nanoscale polarization landscape in the resulting structures regarding the ferroelectric ordering, frustration, non-linear optics, light emission, tunability, and chirality through correlative piezoresponse-force-microscopy (PFM), second-harmonic-generation-microscopy (SHG), and scanning-electron-microscopy-cathodoluminescence (SEM-CL). Phase-field modelling validates the meta-stability of these structures, corroborating experimental data and shedding light on dipole reorganization within frustrated super-boundaries. These findings also provide a promising avenue to explore a broader range of ferroelectric-topological states than previously possible by locally controlling the in-plane ferroelectric polarization on-demand. By designing customized tip-trajectory configurations and integrating them in automated experiments (AE), we anticipate this technique will pioneer new frontiers in ferroic nanolithography.

Hierarchical super-switching

To explore the dynamics of in-plane super-switching, we utilized a 100 nm PSTO thin film. This model ferroelectric material, characterized by a purely in-plane polarization, is grown on a 30 nm $SrRuO_3$ electrode on a $DyScO_3$ (110) single crystal substrate (**Methods**). The resulting PSTO film features a dense in-plane polarized superdomain structure[33,34] consisting of two orthogonal domain orientations (a_1 and a_2), giving rise to four distinct superdomains: II+ (a_1, a_2), II- ($-a_1$, $-a_2$), I+ ($-a_1$, a_2), and I- (a_1, $-a_2$,). The global dipole of each superdomain is aligned along the crystallographic directions [110] (II+), [-1-10] (II-), [-110] (I+), and [1-10] (I-) and demarcated by distinct super-boundaries (**Supplementary Information S1**).

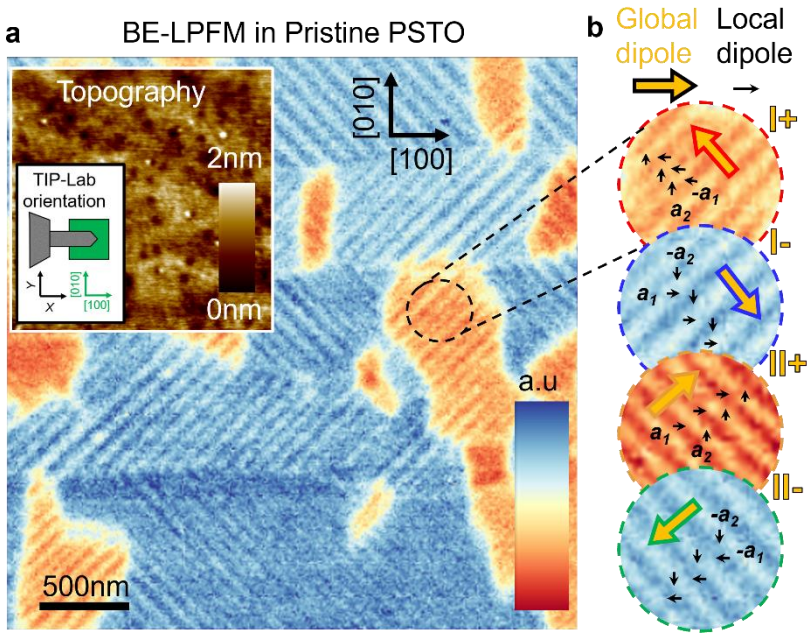

Figure 1: Superdomain structure in PSTO. **a** BE-LPFM image of the pristine sample showing the four distinct superdomain structures. Inset is the surface topography of the same area and relative cantilever-sample orientation. **b** Local (black) and global (yellow) dipole distribution for the four different superdomains (I+. I-, II+ and II-).

The pristine distribution of superdomains is shown (**Figure 1**). The net polarization direction of each superdomain is identifiable as perpendicular to the characteristic a_1/a_2 superlattice stripes present in the lateral PFM images.

Gaining precise control over the local in-plane ferroelectric polarization with an AFM is non-trivial since the electric field from the biased probe in contact with the sample is primarily vertical, but it also possesses lateral components imparting a rotationally invariant applied electric field. Previous research has investigated in-plane super-switching through methods such as pulsing[9,36,37] or raster-scanning[32,38] a biased tip, revealing that it is possible to stabilize single superdomains. The final polar orientation of the superdomains is determined by factors including bias polarity, sample orientation, and the trajectory of the scan path.[32]

To understand the microscopic origins of the superdomain formation, we performed a detailed study where the tip voltage was applied exclusively in one direction of the fast-scan motion (either trace or retrace, **Figure 2a,b**), using standard raster-scan mode. Initially orienting the sample at 45° (such that the slow-scan is aligned along the [110]; **Figure 2c**), we established that (for this configuration) the slow-scan direction drives the overall polarization of the stabilized superdomain, irrespective of the fast-scan direction chosen for voltage application. In this case, it seems that the slow-scan direction drives the superdomain switching by 'pulling' the average net polarization as if it was a single domain, aligning the characteristic stripes/walls parallel to the fast-scan direction. When the sample is oriented at 0° (such that the slow-scan is aligned along the [010]; **Figure 2d**), we observed varying polarizations of the stabilized superdomain for the three different scan paths, highlighting that both the fast- and slow-scanning directions influence the super-switching, when scanning at ±45° angles relative to the pristine superlattice stripes. Specifically, the slow-scan direction shapes the *Y*-axis polarization by aligning the a_2-domain

family, while the fast-scan direction drives the *X*-axis polarization, aligning the a_1-domain family antiparallel to the fast-scan direction and thus fixing a specific domain-wall orientation. This anticipates that the ferroelectric switching in this symmetry configuration is more complex than expected and probably involves a multistep process composed by several local domain rotations, governed primarily by the hierarchical ordering imposed by the material structure (**Supporting Information S2-S4**).

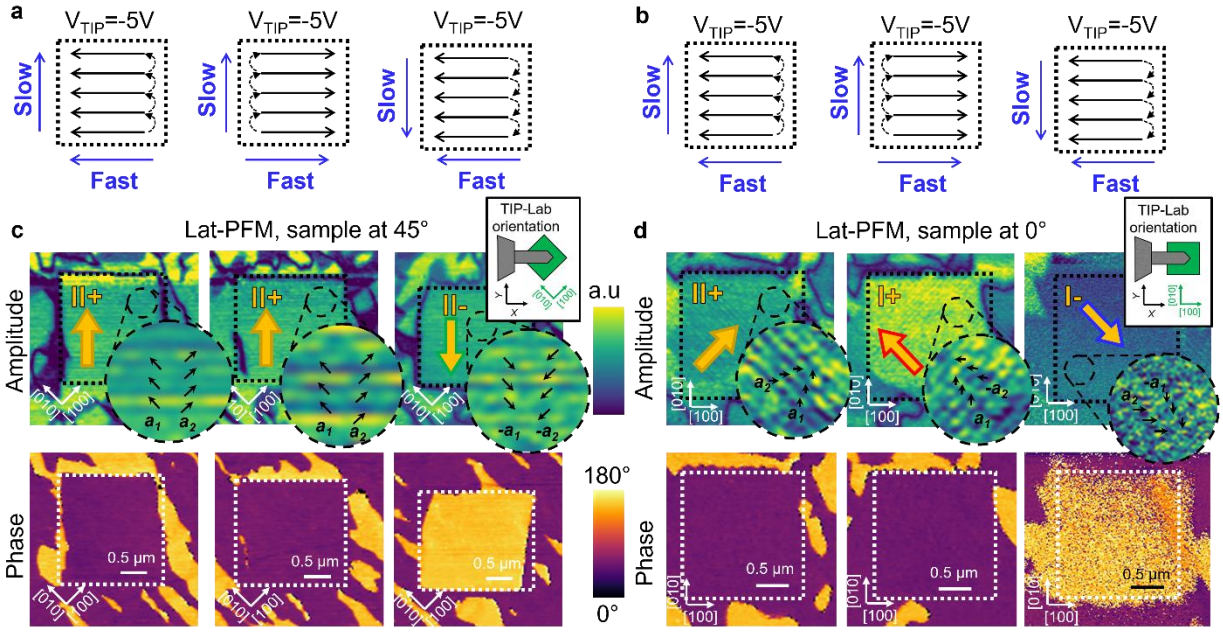

Figure 2: Hierarchical super-switching in PSTO. **a** Illustration of tip bias and scan paths, highlighting slow and fast-scan directions, with the samples main crystallographic axis at 45° relative to the laboratory axes (*X*, *Y*). **b** The arrangement for an orientation of 0°. **c** Lateral PFM amplitude and phase images post raster-scanning, with the sample's crystallographic axis at a 45° angle with respect to the laboratory axes (*X*, *Y*). **d** Corresponding images for a 0° orientation. Insets in **c** and **d** are amplified images to visualize the superlattice direction. The time used for the fast-scan was 1 second per line, which multiplied by 128 lines gives us 2 minutes and 8 seconds for the slow-scan to be completed.

Thus, the super-switching process is not solely dependent on the slow-scan direction, as previously reported[32], challenging the hypothesis of a "trailing" electric field effect. To delve into the switching mechanism, we devise strategic scan trajectories and tailored tip bias waveforms can elucidate the intricacies of such processes, enabling the creation targeted superdomain

configurations on-demand, including topological structures such as center-convergent/divergent or flux-closure.

Nanolithography of convergent/divergent superdomain structures

By precisely controlling the movement of the piezo-positioner during scanning, it becomes possible to guide the probe along any predetermined scan path, enabling the creation of specific topological configurations, not possible using existing scan paths (**Supplementary Information S5**). As shown in the set-up sketch in (**Figure 3a**), we achieved such precise control by integrating a commercially available AFM system with a field programmable gate array (FPGA), controlled externally with custom python programs (AEcroscopy[39]). In the experiments described below, we prepare the surface via standard raster-scanning with a biased tip, aligning the polarization in a specific direction over a large area (~100 μm^2). This process creates a "blank-slate" in one of the four stable superdomain configurations (I-, I+, II-, and II+; **Supplementary Information S6**).

For example, we demonstrate the use of a spiral-scan trajectory (**Figure 3d**) – characterized by a radial slow-scan direction and tangential fast-scan motion – to nucleate and stabilize center-convergent/divergent structures using negative (**Figure 3b,c**) and positive (**Figure 3e,f**) tip biases, respectively. This approach unlocks the combination of the four distinct superdomain orientations into a stable configuration, with the in-plane superdomain dipoles orientated inwards and outwards, respectively, featuring charged internal (and peripheral) super-boundaries. Band excitation lateral PFM (BE-LPFM) reveals the polarization alignment of the generated structure, finding it is not governed by the radial (slow-scanning) direction, since the superdomains are orienting the polarization antiparallel (same direction, opposite sign) to it. As a result, superdomain alignment contrasts with expectations for raster-scanning, where a parallel alignment leading to a center-divergent structure would be expected for a negative bias scan that begins at the center and

traverses outwards radially. Instead, a center-convergent structure is stabilized. Conversely, a positive bias, anticipated to produce a center-convergent structure under the same scanning direction, results in a center-divergent structure .

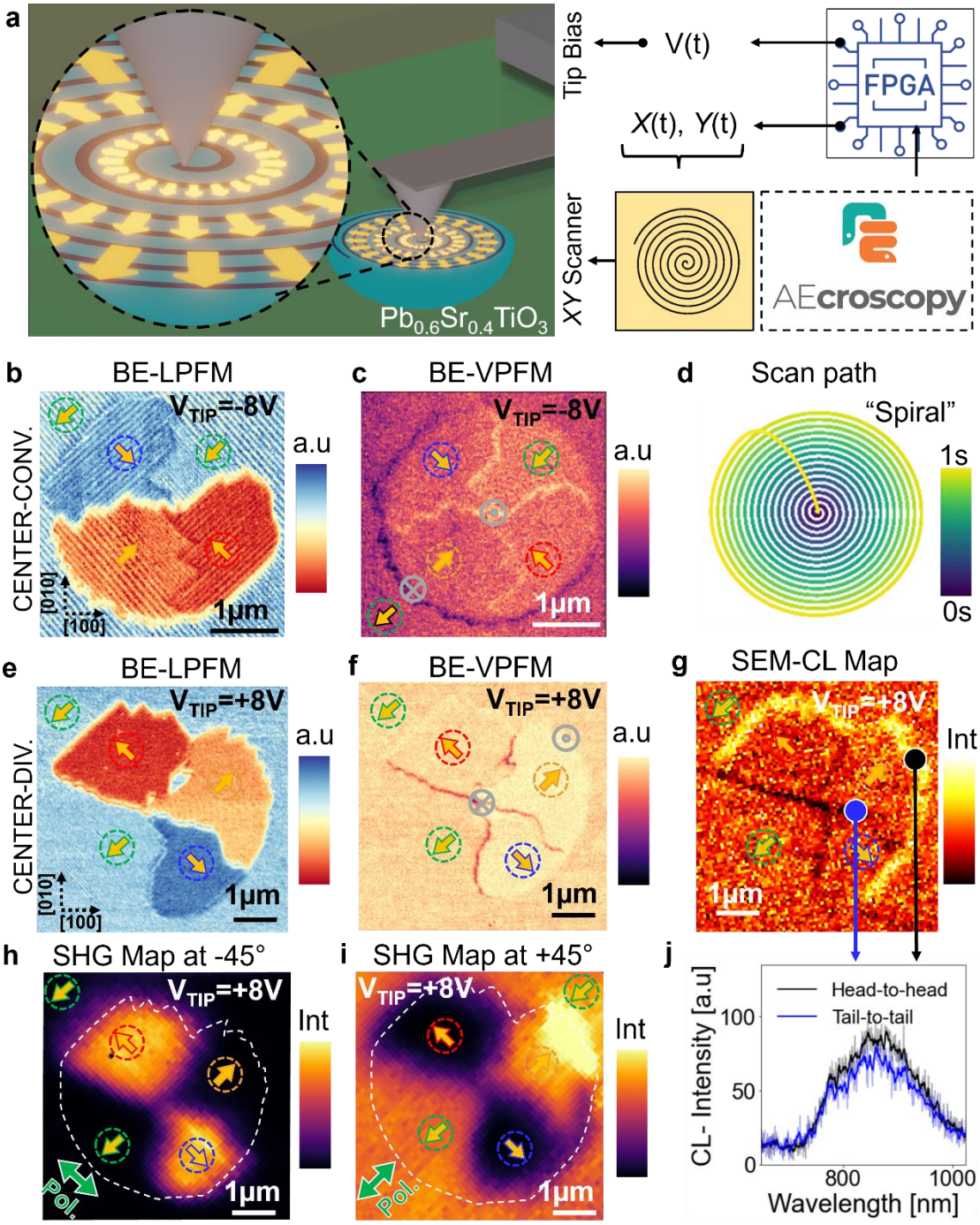

Figure 3: Generation of center-divergent/convergent structures through spiral-scan lithography. **a** Illustration of the experimental setup used for the measurements: AEcroscopy python package controls an FPGA which inputs the signals to the AFM controller to autonomously perform the previously python-designed experiment. **b** BE-LPFM piezoresponse (cantilever long axis parallel to [100] crystallographic axis of the sample) of the written center-convergent structure. **c** BE-VPFM piezoresponse of the written center-convergent structure, grey cross and dot in a circle indicate direction of the out-of-plane components for head-to-head and tail-to-tail. **d** Spiral tip trajectory for the writing of the center convergent structure. **e** BE-LPFM piezoresponse (cantilever long axis parallel to [100] crystallographic axis of the sample) of the written center-divergent structure. **f** BE-VPFM piezoresponse of the written center-divergent structure, grey cross and dot in a circle indicate direction of the out-of-plane components for head-to-head and tail-to-tail. **g** SEM-CL map of the same center-divergent structure. **h** SHG map of the same center divergent structure with the polarizer at -45° (see green arrow). **i** SHG map of the same center divergent structure with the polarizer at +45° (see green arrow). **j** Single SEM-CL spectra at head-to-head and tail-to-tail super-boundaries in the locations indicated by black and blue dots in **g**, respectively.

Interestingly, the corresponding band excitation vertical PFM (BE-VPFM) images (**Figure 3c,f**) reveal an asymmetric vertical contrast at certain super-boundaries. Head-to-head super-boundaries exhibit a positive vertical electromechanical response, while tail-to-tail super-boundaries exhibit negative response, suggesting a local polarization tilting towards positive (and negative) out-of-plane direction at such charged locations, respectively. The lack of conductive-AFM contrast at the super-boundaries (Supplementary Information S7) indicates that these charges observed by KPFM are not mobile (**Supplementary Information S8**).

To explore the structural reorganization effects, we conducted correlative SHG and SEM-CL measurements on the same structures. SHG maps (**Figure 3h,i**) reveal quadrant-specific excitation in center-divergent structures, dictated by the orientation of polarized light adjusted at ±45°. This approach enables precise mapping of local polarization, complementing BE-LPFM data and providing deeper insight into generated super-boundaries. At a polarizer angle of -45° (**Figure 3h**), only quadrants aligned with the incident light's polarization yield measurable SHG signals; at +45° **(Figure 3i**), complementary quadrants display SHG responses along with background. Notably, the +45° image exhibits enhanced SHG response at head-to-head peripheral super-

boundaries, indicating in-plane dipole alignment along the material's [110] axis, alongside observed out-of-plane polarization tilting.

SEM-CL measurements over the same area reveal nanoscale variations in color centers and local polarizations (**Figure 3g**), highlighting imbalanced head-to-head (bright) and tail-to-tail (dark) super-boundaries. The interaction of a focused-electron beam with a ferroelectric material is influenced by luminescent center concentration and localized charge shaping electron beam interactions. The near-infrared CL spectra peaked at 860 nm (**Figure 3j**) maintains consistent shape but varies in emission intensity, suggesting changes in radiative recombination efficiency or light-emitting species concentration. In PSTO, charged defects, such as vacancies and compensating ions, are presumed to asymmetrically stabilize frustrated superdomain configurations. Positively charged head-to-head super-boundaries promote accumulation of charged defects associated with efficient light emission, resulting in stabilized luminescence that favors carrier trapping and boosts radiative recombination processes in these areas.

To deepen our understanding of the stability and polarization reorientation at the frustrated super-boundaries (**Supplementary Information S10-S11**), we performed phase-field simulations (**Figure 4**). We started with initial structures (**Figure 4b, c**) mirroring the superdomain configurations observed before (**Figure 3**), and subsequently allow these structures to relax to an equilibrium state under a tensile strain of 2% (**Methods**). The simulations reveal that the initial configurations indeed relax towards stable arrangements through polarization reorientation to stabilize the high electrostatic/strained super-boundary locations, which are energetically less favorable. Specifically, the tail-to-tail super-boundaries at the center of the center-divergent structures generate a polarization rotation towards the out-of-plane, downward direction (*i.e.*, dark orange, center of **Figure 4d**). Conversely, at the center of the center-convergent structure, the

head-to-head super-boundaries rotate the polarization towards the out-of-plane, upward direction (*i.e.*, light green, center of **Figure 4e**), in agreement with the BE-VPFM contrast found experimentally (**Figure 3**).

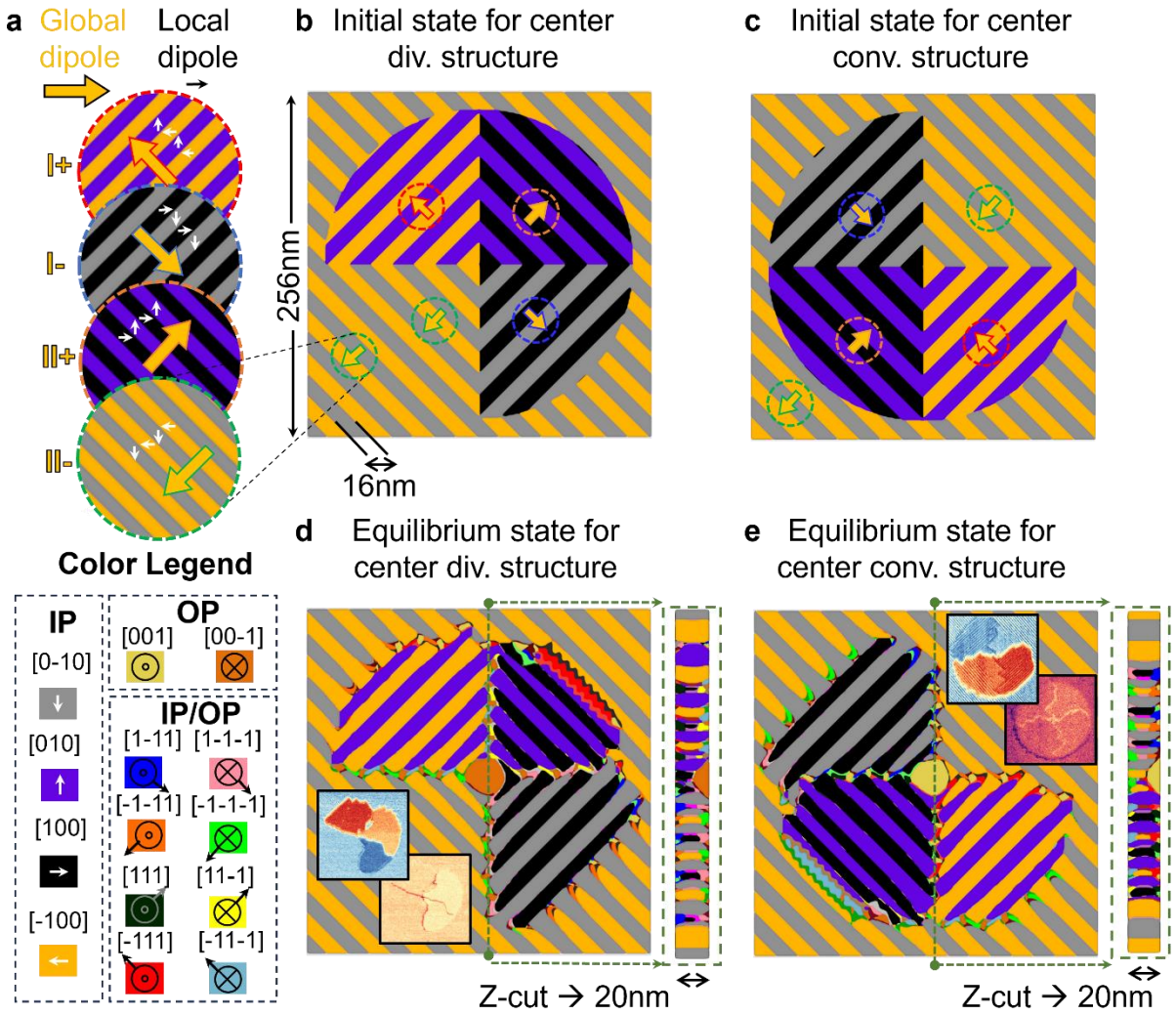

Figure 4: Phase-field modelling of the center-divergent/convergent structures. a Nanoscale arrangement of the global (orange) and local (black) ferroelectric dipoles in the in-plane directions for the 4 different superdomains. Color legend indicating 3D polarization direction for the phase-field structures. **b** Initial state used in the phase-field modelling for the center-divergent structure. **c** Initial state used in the phase-field modelling for the center-convergent structure. **d** Equilibrium state obtained in the phase-field modelling for the center divergent. Inset: experimental BE-LPFM and BE-VPFM of center-divergent structures of **Figure 3**. **e** Equilibrium state obtained in the phase-field modelling for the center-convergent. Inset: experimental BE-LPFM and BE-VPFM of center-convergent structures of **Figure 3**.

Likewise, in all the center-divergent/convergent structures written on a uniform "blank-slate" we find a highly frustrated peripheral super-boundary in one of the four quadrants where the superdomain of the "blank slate" collides with the antiparallel superdomain present in the structure (top-right super-boundary in **Figure 4c**, bottom-left super-boundary in **Figure 4e**). In those cases, we also observe polarization rotation inducing an out-of-plane component of the polarization vector, but in this case with additional in-plane component also present (red and light-blue walls in **Figure 4c**,**e**, respectively), which we hypothesize is responsible for the enhanced SHG signal (**Figure 3i**). Such reorientation also induces the formation of 'sawtooth' faceted super-boundaries to minimize the electrostatic/elastic energies (**Supplementary Information S10-S11**). The simulations indicate that while most of the polarization arrangements are homogeneous through the thickness of the film, the small out-of-plane canting is most prominent near the film surface (cross-sections in **Figure 4c,e**).

Overall, we determine that it is possible to stabilize out-of-plane polarization at the super-boundaries of PSTO through the right accumulation of elastic stress and electrostatic energy, and that this material stabilizes upwards out-of-plane polarization to accommodate the head-to-head super-boundaries and conversely, downward polarization to accommodate the tail-to-tail super-boundaries. Moreover, we suggest that indeed, the in-plane local polarization rotation steps necessary to switch the a_1/a_2 domains may happen through an intermediate out-of-plane rotation[40,41], which would be mediated by the tip vertical electric field, thus becoming the dominant agent of the in-plane super-switching (**Supplementary Information S11**).

As such, we can now revisit the hierarchical super-switching mechanism. The spiral-scan starts in the central point where the vertical electric field nucleates a local out-of-plane polarization (upwards for negative bias and downwards for positive bias) surrounded by a convenient

superdomain arrangement with artificial super-boundaries (head-to-head for negative bias and tail-to-tail for positive bias). In the absence of a scan path, such nucleation centers become unstable due to their small area-to-boundary ratio, and quickly relax when scanned over (**Supplementary Information S12**). Spiral-scanning stabilizes these centers, expanding the super-boundaries via out-of-plane intermediate switching by creating a_1/a_2 stripe domains which are as parallel as possible to the fast-scan direction (tangential) and align appropriately with the nucleated superdomain configuration, generating a global orientation antiparallel to the radial direction. Therefore, we speculate that in this case the stabilized final polarization arrangement is dictated by the sign of the initially nucleated domain in the center, and not by the slow-scan direction, challenging the trailing electric field theory[32,42].

Nanolithography of flux-closure superdomain structures

We employ more exotic scan paths, to generate various topological states, by combining the bias polarity for nucleation, and the propensity of the stripe domains to form tangential to the fast-scan axis to form quadrants that realize flux-closure structures. Accordingly, we design a flower-like scan[39,43] (**Figure 5a**) and explore different permutations**.** The BE-LPFM of a flux-closure structure (**Figure 5b**), written using a negative tip bias on a "blank-slate" area with uniform II- superdomain, shows that it is possible to merge the four permissible superdomain orientations into a stable flux-closure structure, where in-plane dipoles rotate anti-clockwise. The corresponding BE-VPFM of the same structure (**Figure 5c**), reveals vertical contrast at specific super-boundaries, akin to the center-divergent/convergent structures (*i.e.*, out-of-plane tilting upwards for head-to-head and downwards for tail-to-tail super-boundaries). Notably, the internal super-boundaries form a swirl-

like shape (white-dashed line, **Figure 5c**) diverging from the characteristic cross-like shape typical of the center-divergent/convergent structures.

Furthermore, we prove how bias polarity determines the sign of the initial nucleation, generating anticlockwise and clockwise flux-closure domain arrangements with positive and negative biases, respectively (**Figure 5d,e**). We further explore the effect of the scan path's chirality (**Figure 5f**), a mathematical concept based on a structure's distinguishability from its mirror image, critical for stabilizing polar topologies[26,44]. In this case (**Figure 5g**), the slow-scan direction does modify the overall orientation of the generated structure, adding an additional degree of complexity to the stabilization of clockwise or anti-clockwise configurations.

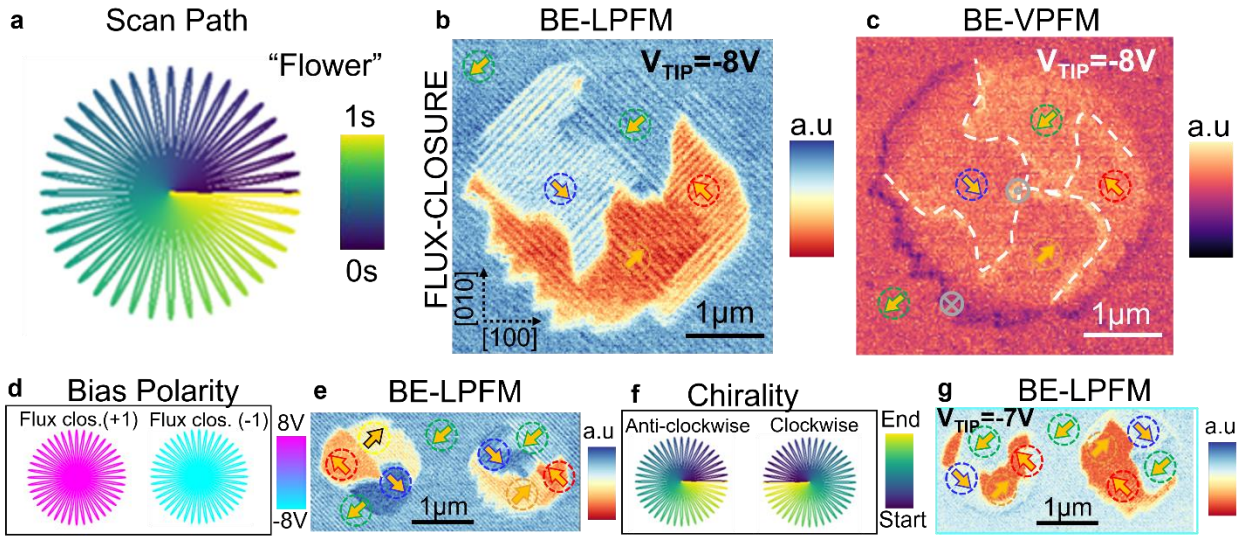

Figure 5: Generation of flux-closure structures through flower-scan lithography. **a** Flower tip trajectory used for the writing. **b** BE-LPFM piezoresponse (cantilever long axis parallel to [100] crystallographic axis of the sample) of the written flux-closure structure. **c** BE-VPFM piezoresponse of the same structure, grey cross and dot in a circle indicate direction of the out-of-plane components for head-to-head and tail-to-tail. . **d** Scan bias polarity used to write the flux-closure states with clockwise and anti-clockwise polarization rotation. **e** BE-LPFM piezoresponse of the structures written using the parameters in **d. f** Scan path with different chirality. **g** BE-LPFM piezoresponse of the written structures with negative bias using the scan paths in f**.**

This effect can be explained by considering all the observations of the super-switching mechanism described in previous sections and summarized elsewhere (**Supplementary**

Information S13). In flower-like trajectories, the fast-scan direction is radial, promoting the growth of a_1/a_2 domains stripes radially. This symmetry is rotated by 90º with respect to the initially nucleated domain configuration, therefore, the flower-like scanning path stabilizes a structure by twisting/dragging the initially nucleated super-boundaries. Interestingly, if the chirality of the flower-scan path used during super-switching is flipped (**Figure 5g** and **Supplementary Information S13g-l**), different flux-closure structures are stabilized, this time with the same bias polarity, demonstrating how handedness plays a crucial role for such chiral arrangements.

On-demand tunability of superdomain nanoengineering

Our approach offers extensive tunability, with numerous adjustable parameters influencing nucleation and domain-dragging processes, including scan path, density, size, writing bias, and duration. Leveraging an AE python-controlled experimental setup we can systematically explore with high reproducibility (Supplementary Information S14) large parameter spaces in an automated fashion, enabling on-demand design and autonomous patterning of structures across the sample surface that can be subsequently read *in-situ* using BE-PFM (**Figure 6)**. For example, we illustrate how bias polarity influences nucleation to produce center-divergent or -convergent structures (**Figure 6a**). Subsequently, BE-LPFM (**Figure 6b**) and BE-VPFM (**Figure 6c**) images showcase domain structures and head-to-head and tail-to-tail super-boundary responses. Varying the tip trajectories sparsity (**Figure 6d**), with spiral paths featuring 16, 8, and 4 internal cycles, impacts the complexity and frustration of the stabilized structures (**Figures 6e,f**). Exploring size-dependence (**Figure 6g**), with spiral sizes ranging from 2000 nm to 250 nm (**Figure 6h**), reveals stabilized structures from microns to hundreds of nanometers in radius (**Figure 6i**), presumably up

to where the area-to-boundary threshold for stabilization of smaller size structures is still fulfilled. Ramping writing bias magnitude, (**Figure 6j**), reveals a coercive voltage between 4V and 6V (**Figure 6k**). Finally, spiral-scan trajectories in clockwise or anti-clockwise directions (**Figure 6l**) reveal no effect on the stabilized structure's handedness (**Figure 6m,n**).

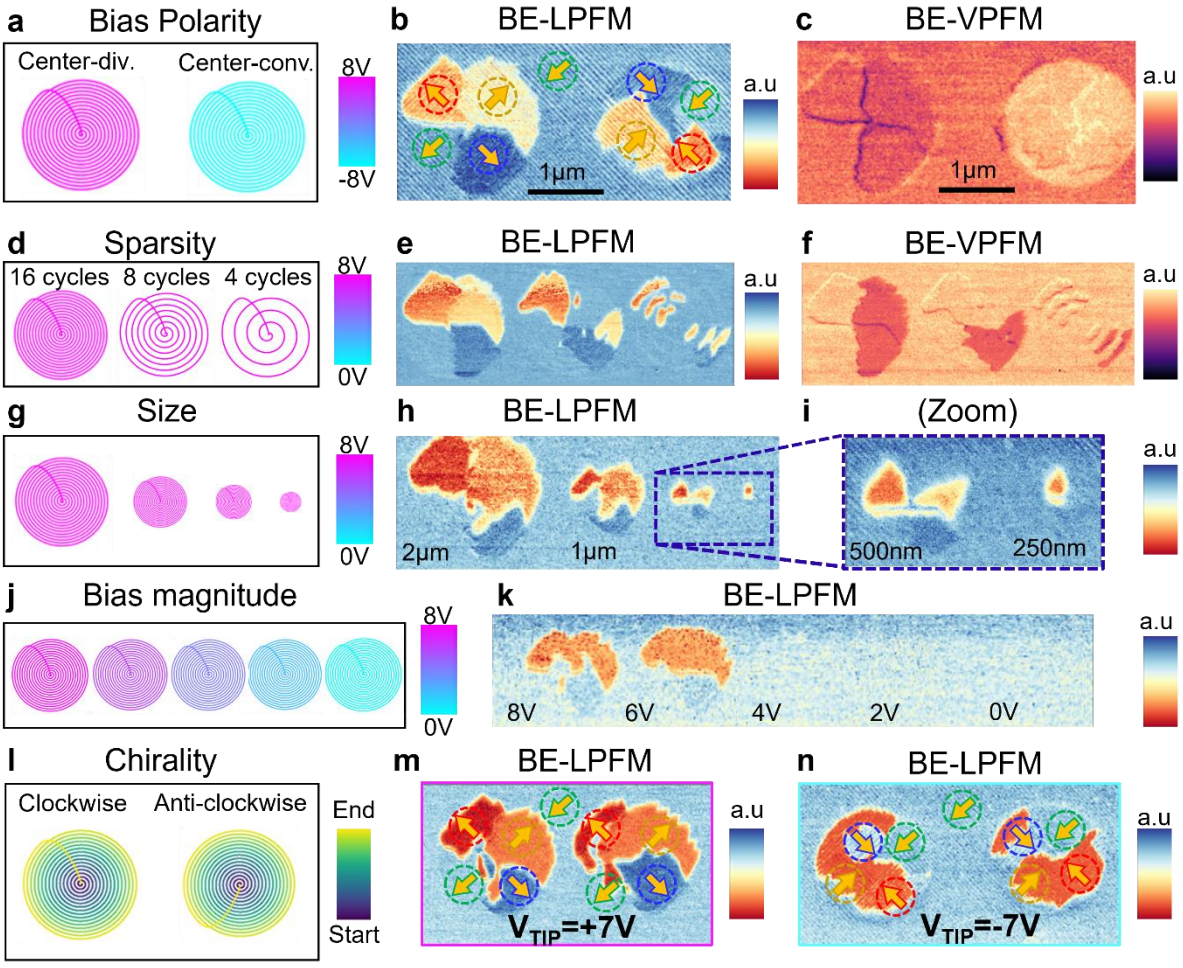

Figure 6: Tunability of the center-convergent/divergent states. **a** Scan bias polarity used to write the center-divergent and -convergent states. **b** BE-LPFM piezoresponse and **c** BE-VPFM piezoresponse of the structures written using the parameters in **a**. **d** Scan paths with different sparsity. **e** BE-LPFM piezoresponse and **f** BE-VPFM piezoresponse of the structures written using the parameters in **d**. **g** Scan path with different size. **h** BE-LPFM piezoresponse and **i** BE-VPFM piezoresponse of the structures written using the parameters in **g**. **j** Scan path with different writing bias magnitude. **k** BE-LPFM piezoresponse of the structures written using the parameters in **j**. **l** Scan path with different chirality/handedness. **m** BE-LPFM piezoresponse of the written structures with positive bias using the scan paths in **l**. **n** BE-LPFM piezoresponse of the written structures with negative bias using the scan paths in **l**.

The number of complex topologies that can be generated using this approach is not limited to the ones shown here. **Supplementary Information S15** shows the generation of shelled center convergent/divergent structures as an additional example. **Supplementary Information S16** shows the generation of snake-like domains exhibiting a "sawtooth" polarization pattern. The relevance of this work relies on the full understanding and subsequent manipulation of super-switching using a biased AFM tip. Combining this knowledge with powerful AE[39,43] (**Supplementary Information S17** shows the implementation of quadrant-dependent bias during the writing process during the generation of square center-divergent/convergent) and machine learning methods, it is readily possible to rapidly design and produce different complex polar topologies or optimize/tune experimental parameters with a desired goal (**Supplementary Information S18**).

Conclusions

Our method has unveiled the intricacies of the super-switching mechanism in in-plane polarized ferroelectric films of PSTO, ruling out the "trailing" field explanation and proposing the appearance of an intermediate out-of-plane state driven by the vertical component of the electric field. This insight has enabled the precise, local manipulation of superdomain structures in an on-demand fashion. By adjusting the scan-path trajectory and other experimental parameters, we can create a plethora of polar topological structures, examine the delicate balance between elastic and electrostatic energies, and study the accommodation of frustrated super-boundaries. Furthermore, correlative microscopy techniques gather the detailed nanometric information needed to inform the phase-field models for evaluating stability and polarization reorganization. Through the design of customized tip-trajectory configurations and their implementation in AE, this work forges a new

frontier in nanolithography for ferroics, enabling the exploration of significantly more ferroelectric topological states than previously were capable of being synthesized.

Methods:

Sample preparation

The films studied in this work were produced with pulsed-laser deposition using a KrF excimer laser (248 nm, LPX 300, Coherent). The work here focuses on heterostructures of the form 100 nm $Pb_{0.6}Sr_{0.4}TiO_3$/30 nm $SrRuO_3$/$DyScO_3$(110) (CrysTecGmbH) using established procedures[33,34]. The $SrRuO_3$ growth was carried out first at a heater temperature of 690°C in a dynamic oxygen pressure of 100 mTorr with a laser fluence of 1 J/cm^2 and a laser repetition rate of 17 Hz from a ceramic target (Praxair) of the same composition. Following that growth, the $Pb_{0.6}Sr_{0.4}TiO_3$ growth was carried out at a heater temperature of 625°C in a dynamic oxygen pressure of 200 mTorr with a laser fluence of 1.9 J/cm^2. The laser repetition rates of 10 and 2Hz were used for the $Pb_{1.1}TiO_3$ ceramic target (Praxair) and the $SrTiO_3$ single crystal target, respectively. The desired composition was achieved via subunit cell-level material mixing using the synchronized targets motion and laser pulse sequence. The 10% excess lead in the $Pb_{1.1}TiO_3$ target was found to be vital to compensate the lead loss during growth. Following the growth, the samples were cooled to room temperature at 10°C/min in a static oxygen pressure of 700 Torr. The as-grown films were also characterized by X-ray diffraction including symmetric θ-2θ line scans, rocking curves, and 2D reciprocal space mapping (RSM) studies using a high-resolution X-ray diffraction (XRD) X'pert Pro2, PANalytical system (**Supplementary Information S19**). All films studied herein were found to be highly crystalline and fully epitaxial.

Writing the topological structures

Arbitrary path scanning of the AFM probe is accomplished by employing a Cypher AFM system (from Asylum Research, an Oxford Instruments company) controlled through an FPGA using a

custom LabVIEW/Python interface. This interface directs the tip's movement along any desired trajectory, by inputing the desired waveforms directly to the XY piezoscanners of the commercial AFM (see **Supplementary Information S4** and other works[45,46]). The tips utilized are commercially available Multi75-G (BudgetSensors) with a free resonance frequency of 75 kHz and a spring constant of 3 N m−1.

Reading the topological structures

BE-PFM was performed using external data acquisition electronics based on a NI-6115 fast DAQ card controlled by custom-built LabVIEW software. A chirp voltage signal around the 1st cantilever contact resonance frequency (≈350kHz) or the torsional contact resonance frequency (≈650kHz), was applied to the AFM probe while the sample was grounded, for vertical and lateral polarization reading, respectively. The PFM experimental data were stored in h5 files and post processed using the python pycroscopy package[47]. LPFM images at orthogonal cantilever orientations are shown in **Supplementary Information S20**, where the different in-plane components can be studied for the same area of the sample.

Phase-field simulations

To perform the phase-field simulations, we selected $PbTiO_3$ as a ferroelectric thin film for our model. We employed a polarization vector $P_i = (P_x, P_y, P_z)$ as an order parameter to denote the state of polarization along x, y, and z-directions in the global coordinates system. The total free energy density of the system can be expressed by the following equation,

$$F = \int_V \left\{ f_{grad}\left(P_{i,j}\right) + f_{bulk}(P_i) + f_{elec}\,(P_i, E_i) + f_{elas}\left(P_i, \varepsilon_{ij}\right) \right\} dV \qquad (1)$$

Where f_{elas}, f_{grad}, f_{bulk}, and f_{elec} denote elastic energy, gradient energy, bulk energy, and electrostatic energy, respectively. V is the total volume of the system. E_i and ε_{ij} are the components of the electric field and elastic strain, respectively. A detailed explanation of each energy density in Equation (1) can be found in the literature[48].

The temporal evolution of the polarization vector P_i is calculated by solving the time-dependent Landau-Ginzburg-Devonshire (LGD) equation,

$$\frac{\partial P_i(x,t)}{\partial t} = -L\frac{\partial F}{\partial P_i(x,t)}, (i = 1-3) \qquad (2)$$

Where t is time, x is the spatial position, and L is a kinetic coefficient related to the mobility of the domain wall.

The simulation was done using a realistic 3D geometry and the system size was chosen to be $256\Delta x \times 256\Delta y \times 32\Delta z$, with $\Delta x = \Delta y = \Delta z = 1nm$. The thickness of the substrate, air, and film are $10\ nm$, $2\ nm$, and $20\ nm$, respectively. Substrate strain was set at 2% to stabilize the structure properly, and the simulation was performed at room temperature. Periodic boundary conditions were applied along in-plane directions (x and y), whereas proper mechanical and electrical boundary conditions were applied along out-of-plane (z) directions. The isotropic relative dielectric coefficient k_{ii} is set to be 50, while the gradient energy coefficients are chosen to be $\frac{G_{11}}{G_{110}} = 0.6$, where $G_{110} = 1.73 \times 10^{-10}\ C^{-2}m^4N$. Other constants such as Landau coefficients, elastic-compliance, and electrostrictive coefficients are taken from the literature[49].

Second Harmonic Generation Microscope

In SHG, a linearly polarized laser light at a frequency ω is focused onto the sample and the reflected light at the frequency 2ω is detected accounting for the non-linear light-matter interactions

occurring in non-centrosymmetric materials. By raster-scanning the excitation laser and collecting spectra at each location, spatial maps of the polarization orientation relative to the incident excitation polarization can be obtained. The SHG measurements were conducted using a 100 fs Ti:Sapphire laser (Mai Tai HP, Spectra Physics) at 800 nm and 80 MHz repetition rate. The laser beam was passed through a half-wave plate mounted in a rotation stage and was directed into an upright microscope (Olympus) and focused onto a sample surface using a 100x microscope objective (Numerical Aperture: NA=0.9) to a ~1.1 μm diameter spot. The laser energy at the sample surface was 0.8 mW. The SHG light was collected in backscattering configuration using the same objective and was directed to a monochromator (Spectra Pro 2300i, Acton, f = 0.3 m) that was coupled to the microscope and equipped with a 150 grooves/mm grating and a CCD camera (Pixis 256BR, Princeton Instruments). Before entering the monochromator, the SHG light was passed through a short-pass cut-off filter (650 nm) to filter out the fundamental excitation light at 800 nm and a polarizer to select SHG polarization colinear or cross relative to the polarization of the excitation light. A motorized computer controlled XY microscope stage (Marzhauser) with minimum scanning steps of 100 nm was used to perform SHG mapping. Polarization resolved measurements were performed by inserting a computer controlled rotational stage with a broad-band half-wave plate into excitation and back-scattered SHG beam paths.

Scanning Electron Microscopy Cathodoluminescence

Cathodoluminescence (CL) spectra were obtained using an FEI Quattro environmental SEM equipped with a Delmic Sparc CL collection module. This setup enabled concurrent acquisition of secondary electron signals and CL spectra for spatially resolved analyses. Measurements were

performed with an electron accelerating voltage of 5 kV and a beam current of 230 pA over a square scan area of 7.2x7.2 μm^2 with a chosen pixel density of 125x125.

Data availability

The data that support the findings of this study are available from the corresponding author upon request.

Code availability.

Python scripts used for the analysis are available in Github (https://github.com/mchecanu/Topological_ferroelectrics) and Zenodo[50].

References

1 Chen, S. *et al.* Recent Progress on Topological Structures in Ferroic Thin Films and Heterostructures. *Advanced Materials* **33**, 2000857, doi:https://doi.org/10.1002/adma.202000857 (2021).

2 Catalan, G., Seidel, J., Ramesh, R. & Scott, J. F. Domain wall nanoelectronics. *Reviews of Modern Physics* **84**, 119 (2012).

3 Marković, D., Mizrahi, A., Querlioz, D. & Grollier, J. Physics for neuromorphic computing. *Nature Reviews Physics* **2**, 499-510, doi:10.1038/s42254-020-0208-2 (2020).

4 Junquera, J. *et al.* Topological phases in polar oxide nanostructures. *Reviews of Modern Physics* **95**, 025001 (2023).

5 McConville, J. P. V. *et al.* Ferroelectric Domain Wall Memristor. *Advanced Functional Materials* **30**, 2000109, doi:https://doi.org/10.1002/adfm.202000109 (2020).

6 Seidel, J. *et al.* Conduction at domain walls in oxide multiferroics. *Nature Materials* **8**, 229-234, doi:10.1038/nmat2373 (2009).

7 Luk'yanchuk, I., Tikhonov, Y., Razumnaya, A. & Vinokur, V. M. Hopfions emerge in ferroelectrics. *Nature Communications* **11**, 2433, doi:10.1038/s41467-020-16258-w (2020).

8 Wang, J. *et al.* Polar Solomon rings in ferroelectric nanocrystals. *Nature Communications* **14**, 3941, doi:10.1038/s41467-023-39668-y (2023).

9 Balke, N. *et al.* Deterministic control of ferroelastic switching in multiferroic materials. *Nature nanotechnology* **4**, 868-875 (2009).

10 Balke, N. *et al.* Enhanced electric conductivity at ferroelectric vortex cores in BiFeO3. *Nature Physics* **8**, 81-88 (2012).

11 Winkler, R. S. *et al.* Electromechanical Manipulation of Topological Defects to Yield Giant Piezoelectric Response in Epitaxial Lead Zirconate Titanate Bilayers on Silicon.

Advanced Electronic Materials **7**, 2100195, doi:https://doi.org/10.1002/aelm.202100195 (2021).
12 Das, S. *et al.* Observation of room-temperature polar skyrmions. *Nature* **568**, 368-372 (2019).
13 Zhang, H.-Y. *et al.* Observation of Vortex Domains in a Two-Dimensional Lead Iodide Perovskite Ferroelectric. *Journal of the American Chemical Society* **142**, 4925-4931, doi:10.1021/jacs.0c00371 (2020).
14 Yadav, A. K. *et al.* Observation of polar vortices in oxide superlattices. *Nature* **530**, 198-201 (2016).
15 Gradauskaite, E. *et al.* Defeating depolarizing fields with artificial flux closure in ultrathin ferroelectrics. *Nature Materials*, doi:10.1038/s41563-023-01674-2 (2023).
16 Das, S. *et al.* Observation of room-temperature polar skyrmions. *Nature* **568**, 368-372, doi:10.1038/s41586-019-1092-8 (2019).
17 Han, L. *et al.* High-density switchable skyrmion-like polar nanodomains integrated on silicon. *Nature* **603**, 63-67, doi:10.1038/s41586-021-04338-w (2022).
18 Tang, Y. L. *et al.* Observation of a periodic array of flux-closure quadrants in strained ferroelectric PbTiO₃ films. *Science* **348**, 547-551, doi:doi:10.1126/science.1259869 (2015).
19 Wang, Y. J. *et al.* Polar meron lattice in strained oxide ferroelectrics. *Nature Materials* **19**, 881-886, doi:10.1038/s41563-020-0694-8 (2020).
20 Sánchez-Santolino, G. *et al.* A 2D ferroelectric vortex pattern in twisted BaTiO3 freestanding layers. *Nature* **626**, 529-534, doi:10.1038/s41586-023-06978-6 (2024).
21 Ma, J. *et al.* Controllable conductive readout in self-assembled, topologically confined ferroelectric domain walls. *Nature Nanotechnology* **13**, 947-952, doi:10.1038/s41565-018-0204-1 (2018).
22 Yang, W. *et al.* Quasi-one-dimensional metallic conduction channels in exotic ferroelectric topological defects. *Nature communications* **12**, 1306 (2021).
23 Vasudevan, R. K. *et al.* Exploring Topological Defects in Epitaxial BiFeO3 Thin Films. *ACS Nano* **5**, 879-887, doi:10.1021/nn102099z (2011).
24 Gao, Z. *et al.* Mechanical manipulation for ordered topological defects. *Science Advances* **10**, eadi5894, doi:doi:10.1126/sciadv.adi5894 (2024).
25 Guo, M. *et al.* Electrically and mechanically driven rotation of polar spirals in a relaxor ferroelectric polymer. *Nature Communications* **15**, 348 (2024).
26 Shao, Y.-T. *et al.* Emergent chirality in a polar meron to skyrmion phase transition. *Nature Communications* **14**, 1355, doi:10.1038/s41467-023-36950-x (2023).
27 Balke, N. *et al.* Deterministic control of ferroelastic switching in multiferroic materials. *Nature Nanotechnology* **4**, 868-875 (2009).
28 Wu, H. *et al.* Magnetic memory driven by topological insulators. *Nature Communications* **12**, 6251, doi:10.1038/s41467-021-26478-3 (2021).
29 Domingo, N. Bowing to ferroelectric artificial flux closure. *Nature Materials* **22**, 1441-1443 (2023).
30 Scott, J. F. *et al.* Superdomain dynamics in ferroelectric-ferroelastic films: switching, jamming, and relaxation. *Applied Physics Reviews* **4** (2017).
31 McQuaid, R. G., Gruverman, A., Scott, J. F. & Gregg, J. M. Exploring vertex interactions in ferroelectric flux-closure domains. *Nano letters* **14**, 4230-4237 (2014).

32 Matzen, S. *et al.* Super switching and control of in-plane ferroelectric nanodomains in strained thin films. *Nature Communications* **5**, 4415, doi:10.1038/ncomms5415 (2014).

33 Kavle, P. *et al.* Strain-Driven Mixed-Phase Domain Architectures and Topological Transitions in Pb1− xSrxTiO3 Thin Films. *Advanced Materials* **34**, 2203469 (2022).

34 Kavle, P. *et al.* Exchange-Interaction-Like Behavior in Ferroelectric Bilayers. *Advanced Materials* **35**, 2301934 (2023).

35 Chen, C. *et al.* Deterministic Manipulation of Multi-State Polarization Switching in Multiferroic Thin Films. *Advanced Functional Materials* **33**, 2208244, doi:https://doi.org/10.1002/adfm.202208244 (2023).

36 Kelley, K. P. *et al.* Probing Metastable Domain Dynamics via Automated Experimentation in Piezoresponse Force Microscopy. *ACS Nano* **15**, 15096-15103, doi:10.1021/acsnano.1c05455 (2021).

37 Vasudevan, R. K. *et al.* Exploring topological defects in epitaxial BiFeO3 thin films. *Acs Nano* **5**, 879-887 (2011).

38 Wu, M. *et al.* Facile Control of Ferroelastic Domain Patterns in Multiferroic Thin Films by a Scanning Tip Bias. *ACS Applied Materials & Interfaces* **15**, 11983-11993, doi:10.1021/acsami.2c20106 (2023).

39 Liu, Y. *et al.* AEcroscopy: A Software–Hardware Framework Empowering Microscopy Toward Automated and Autonomous Experimentation. *Small Methods* **n/a**, 2301740, doi:https://doi.org/10.1002/smtd.202301740.

40 Fedorova, N. S. *et al.* Understanding magnetoelectric switching in BiFeO 3 thin films. *Physical Review B* **109**, 085116 (2024).

41 Heron, J. T. *et al.* Deterministic switching of ferromagnetism at room temperature using an electric field. *Nature* **516**, 370-373, doi:10.1038/nature14004 (2014).

42 Wu, M. *et al.* Complete Selective Switching of Ferroelastic Domain Stripes in Multiferroic Thin Films by Tip Scanning. *Advanced Electronic Materials* **n/a**, 2300640, doi:https://doi.org/10.1002/aelm.202300640.

43 Liu, Y., Checa, M. & Vasudevan, R. K. Synergizing human expertise and AI efficiency with language model for microscopy operation and automated experiment design*. *Machine Learning: Science and Technology* **5**, 02LT01, doi:10.1088/2632-2153/ad52e9 (2024).

44 Behera, P. *et al.* Electric field control of chirality. *Science advances* **8**, eabj8030 (2022).

45 Checa, M. *et al.* High-speed mapping of surface charge dynamics using sparse scanning Kelvin probe force microscopy. *Nature Communications* **14**, 7196, doi:10.1038/s41467-023-42583-x (2023).

46 Checa, M., Kelley, K., Vasudevan, R., Collins, L. & Jesse, S. Automated piezoresponse force microscopy domain tracking during fast thermally stimulated phase transition in CuInP2S6. *Nanotechnology* **34**, 325703 (2023).

47 Somnath, S., Smith, C. R., Laanait, N., Vasudevan, R. K. & Jesse, S. USID and Pycroscopy – Open Source Frameworks for Storing and Analyzing Imaging and Spectroscopy Data. *Microscopy and Microanalysis* **25**, 220-221, doi:10.1017/S1431927619001831 (2019).

48 Zhang, H. *et al.* Strain phase diagram and physical properties of (110)-oriented PbTiO3 thin films by phase-field simulations. *Acta Materialia* **228**, 117761, doi:https://doi.org/10.1016/j.actamat.2022.117761 (2022).

49 Haun, M. J., Furman, E., Jang, S., McKinstry, H. & Cross, L. Thermodynamic theory of PbTiO3. *Journal of Applied Physics* **62**, 3331-3338 (1987).

50 Repository: Topological_ferroelectrics (2024).

Acknowledgements

Experimental research was supported by the Center for Nanophase Materials Sciences, (CNMS), which is a US Department of Energy, Office of Science User Facility at Oak Ridge National Laboratory. This manuscript has been authored by UT-Battelle, LLC, under Contract No. DEAC0500OR22725 with the U.S. Department of Energy. P.K. acknowledges the support of the Army Research Office under the ETHOS MURI via cooperative agreement W911NF-21-2-0162 and the Intel Corp. via the COFEEE program. A.D. acknowledges the support of the National Science Foundation via Grant DMR-2102895. L.W.M. acknowledges the support of the National Science Foundation via Grant DMR-2329111. Y.C. acknowledges the support of the National Science Foundation via Grant CMMI-2132105.

Author contributions

M.C., K.K, and N.D conceived the research. M.C. designed and performed the writing of the structures and PFM measurements. A.P performed the SHG measurements. B.D performed the SEM-CL measurements. B.P and Y.C performed the phase-field modelling. S.J. built the LabVIEW code needed to interconnect the python interface with the AFM. R.V assisted in the python coding and interpretation of the results. Y.L performed the Gaussian process optimization. K.K, L.C, RV and N.D provided experimental support and helped in the interpretation of the results. M.C. prepared the figures and wrote the manuscript with support of all the co-authors.